

Deciphering the contributing motifs of reconstructed cobalt (II) sulfides catalysts in Li-CO₂ batteries

Received: 30 May 2023

Accepted: 27 February 2024

Published online: 09 March 2024

Check for updates

Yingqi Liu^{1,7}, Zhiyuan Zhang^{1,7}, Junyang Tan¹, Biao Chen², Bingyi Lu¹, Rui Mao¹, Bilu Liu¹, Dashuai Wang³✉, Guangmin Zhou¹✉ & Hui-Ming Cheng^{4,5,6}✉

Developing highly efficient catalysts is significant for Li-CO₂ batteries. However, understanding the exact structure of catalysts during battery operation remains a challenge, which hampers knowledge-driven optimization. Here we use X-ray absorption spectroscopy to probe the reconstruction of CoS_x (x = 8/9, 1.097, and 2) pre-catalysts and identify the local geometric ligand environment of cobalt during cycling in the Li-CO₂ batteries. We find that different oxidized states after reconstruction are decisive to battery performance. Specifically, complete oxidation on CoS_{1.097} and Co₉S₈ leads to electrochemical performance deterioration, while oxidation on CoS₂ terminates with Co-S₄-O₂ motifs, leading to improved activity. Density functional theory calculations show that partial oxidation contributes to charge redistributions on cobalt and thus facilitates the catalytic ability. Together, the spectroscopic and electrochemical results provide valuable insight into the structural evolution during cycling and the structure-activity relationship in the electrocatalyst study of Li-CO₂ batteries.

The overreliance on fossil fuels has significantly increased atmospheric CO₂ levels, which poses a severe threat to the environment and the survival of humankind¹. To mitigate global warming and climate change, it is vital to develop carbon-neutral technologies, including CO₂-related technology, clean energy technology, as well as high energy-density energy storage systems^{2–4}. Recently, Li-CO₂ batteries have emerged as an attractive solution due to their dual functions of energy storage capability and CO₂ recyclability^{5–9}. Based on the reaction $4\text{Li} + 3\text{CO}_2 \leftrightarrow 2\text{Li}_2\text{CO}_3 + \text{C}$, Li-CO₂ batteries have a high theoretical potential of 2.8 V vs Li/Li⁺ and a theoretical energy density of 1876 Wh kg⁻¹. However, the sluggish kinetics of CO₂ reactions cause unsatisfactory electrochemical performance, such as high

overpotential, poor reversibility, low energy efficiency, etc. Therefore, there is a critical need to develop highly efficient catalysts that can unlock the full potential of this emerging technology^{3,10–13}.

Transition metal sulfides show superior catalytic abilities in Li-CO₂ batteries as shown in Fig. 1a and Supplementary Table 1^{10,14–41}. However, these sulfide catalysts are susceptible to irreversible reconstruction, particularly oxidation, due to their thermodynamic instability. In Li-CO₂ batteries, the main discharge product is Li₂CO₃, whose decomposition may generate singlet O₂ or superoxide radicals during charging^{9,42–45}. The formation of these aggressive oxygen species can exacerbate oxidation phenomena, influencing the activity of sulfides based on their reconstructed structures and oxidized states. Complete

¹Tsinghua-Berkeley Shenzhen Institute & Tsinghua Shenzhen International Graduate School, Tsinghua University, Shenzhen 518055, PR China. ²School of Materials Science and Engineering and Tianjin Key Laboratory of Composite and Functional Materials, Tianjin University, Tianjin 300350, PR China. ³Institute of Zhejiang University-Quzhou & Key Laboratory of Biomass Chemical Engineering of Ministry of Education, College of Chemical and Biological Engineering, Zhejiang University, Hangzhou 310027, China. ⁴Shenyang National Laboratory for Materials Science, Institute of Metal Research, Chinese Academy of Sciences, Shenyang 110016, China. ⁵Institute of Technology for Carbon Neutrality, Shenzhen Institute of Advanced Technology, Chinese Academy of Sciences, Shenzhen 518055, PR China. ⁶Shenzhen University of Advanced Technology, Shenzhen 518055, China. ⁷These authors contributed equally: Yingqi Liu, Zhiyuan Zhang. ✉e-mail: dswang@zju.edu.cn; guangminzhou@sz.tsinghua.edu.cn; hm.cheng@siat.ac.cn; cheng@imr.ac.cn

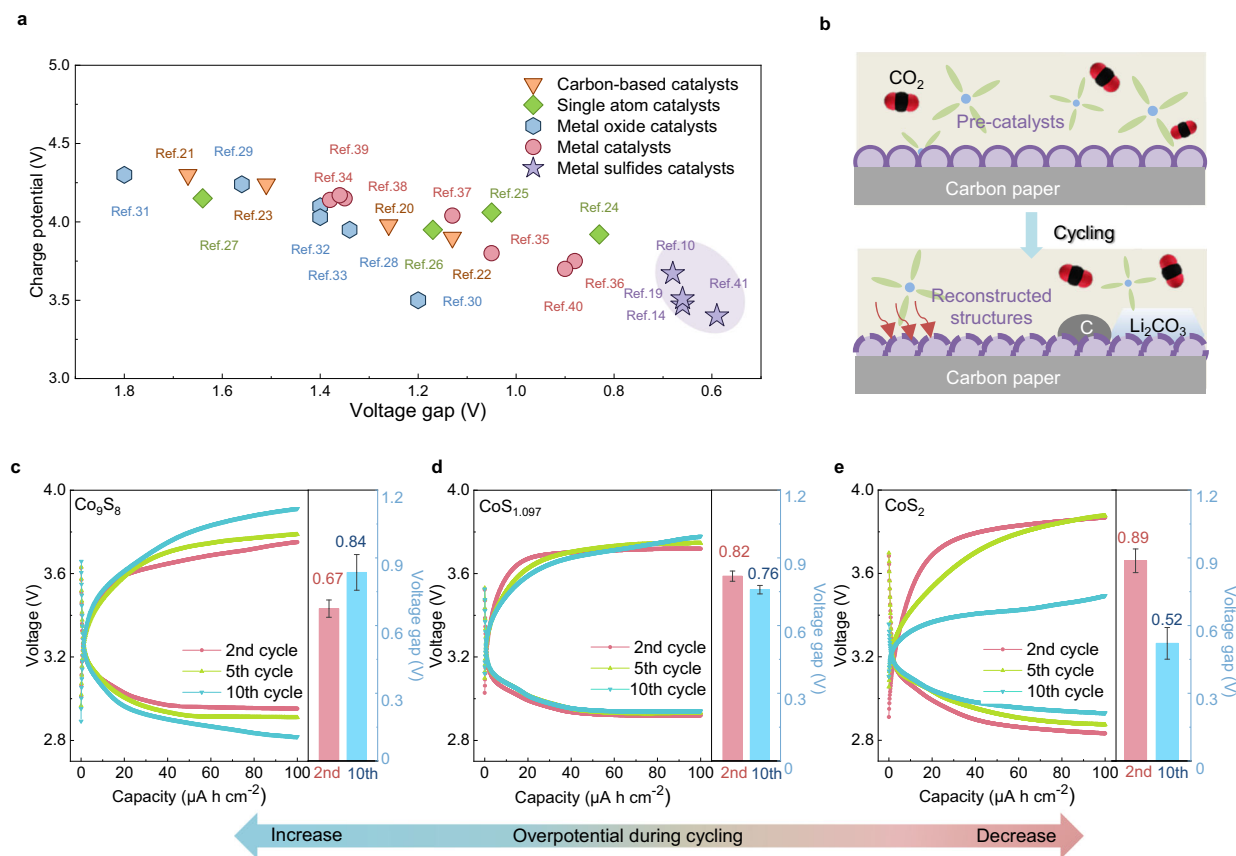


Fig. 1 | Electrochemical behaviors of CoS_x during cycling. **a** Performance comparison of reported catalysts. (Carbon-based catalysts reported in refs. 20–23.; Single-atom catalysts reported in refs. 24–27.; Metal oxide catalysts reported in refs. 28–33; Metal catalysts reported in ref. 34–40; Metal sulfide catalysts reported in refs. 10,14,19,41) **b** Schematic of catalyst reconstruction in Li-CO₂ batteries.

Discharge and charge curves of **c** Co₉S₈, **d** CoS_{1.097}, and **e** CoS₂ with a limited capacity of 100 μA h cm⁻² at a rate of 20 μA cm⁻². Error bars of the voltage gap represent the standard deviation from three independent measurements. Source data are provided as a Source Data file.

oxidation typically induces structural changes and widens the band gap, similar to oxides, thereby significantly reducing activity. Conversely, oxysulfides sometimes exhibit higher stability and activity compared to sulfides, making them more appealing^{46,47}. Therefore, it is crucial to consider sulfides as pre-catalysts, investigate their structural reconstruction, assess the impact of oxygen during cycling, and identify the actual active structures (Fig. 1b). This will help understand active motifs and intrinsic properties in structural adaptation under battery operation, enabling the development of advanced catalysts for Li-CO₂ batteries. Nevertheless, little attention has been given to it so far.

To address the critical aspects mentioned above, we investigate the electrochemical performance and structural evolution of three types of cobalt (II) sulfide pre-catalysts (CoS_x, $x = 8/9, 1.097, \text{ and } 2$) in Li-CO₂ batteries. We find that the CoS₂ cathode has a reduced overpotential, while CoS_{1.097} and Co₉S₈ do not show the same decrease during cycling. The spectroscopic analysis indicates that the oxidation of the CoS₂ cathode terminates with Co-S₄-O₂ motifs while CoS_{1.097} and Co₉S₈ are completely oxidized with a structure similar to CoO in Li-CO₂ batteries. Supported by titration results, we propose that the oxidation states after reconstruction are affected by side reactions during charge on the pre-catalyst. Density functional theory (DFT) calculations revealed that partial oxygen substitution modulates the electronic structure and shifts the *d*-band center to higher energy, thus improving the catalytic ability of CoS₂. Hence, CoS₂ has a high performance with an overpotential of 0.43 V after 400 h, while the overpotentials of CoS_{1.097} and Co₉S₈ cathodes exceed 2 V after only 200 h in Li-CO₂ batteries. This work provides insights into catalyst reconstruction

under complex environments and contributes significantly to understanding the inherent structure-activity relationship in Li-CO₂ batteries.

Results and discussion

Structure characterizations and electrochemical behaviors of CoS_x

The CoS_x ($x = 8/9, 1.097, \text{ and } 2$) samples were synthesized by sulfidation of Co(OH)₂ nanosheet arrays electrodeposited on pieces of carbon papers (CP) (Supplementary Fig. 1). Their X-ray diffraction (XRD) patterns in Supplementary Fig. 2 contain diffraction peaks that match those of standard CoS₂, CoS_{1.097}, and Co₉S₈ except for peaks at about 26°, 43° and 55°(2θ), which correspond to the CP substrate^{7,14,48}. The morphologies of the as-prepared CoS_x were studied using scanning electron microscopy (SEM). Supplementary Fig. 3a–d show that CoS₂, CoS_{1.097}, and Co₉S₈ maintain a similar nanosheet structure to electrodeposited Co(OH)₂. Supplementary Fig. 4 also confirms that the electrochemical surface active area (ECSA) of the three cathodes is similar, ruling out their influence on the following electrochemical test. The high-resolution transmission electron microscopy (HRTEM) images in Supplementary Fig. 5a–c show three sets of lattice fringes, with interplanar spacings of 0.28 nm, 0.29 nm, and 0.30 nm, which can be assigned to (200), (204), and (311) planes of CoS₂, CoS_{1.097}, and Co₉S₈, respectively. Element mappings in Supplementary Fig. 6a–c confirm the uniform distribution of Co and S. Their electrochemical behaviors exhibit notable differences in Li-CO₂ batteries, as shown in Fig. 1c–e and Supplementary Fig. 7. Batteries with Co₉S₈ cathodes show an increase in overpotential, while the discharge and charge curves for

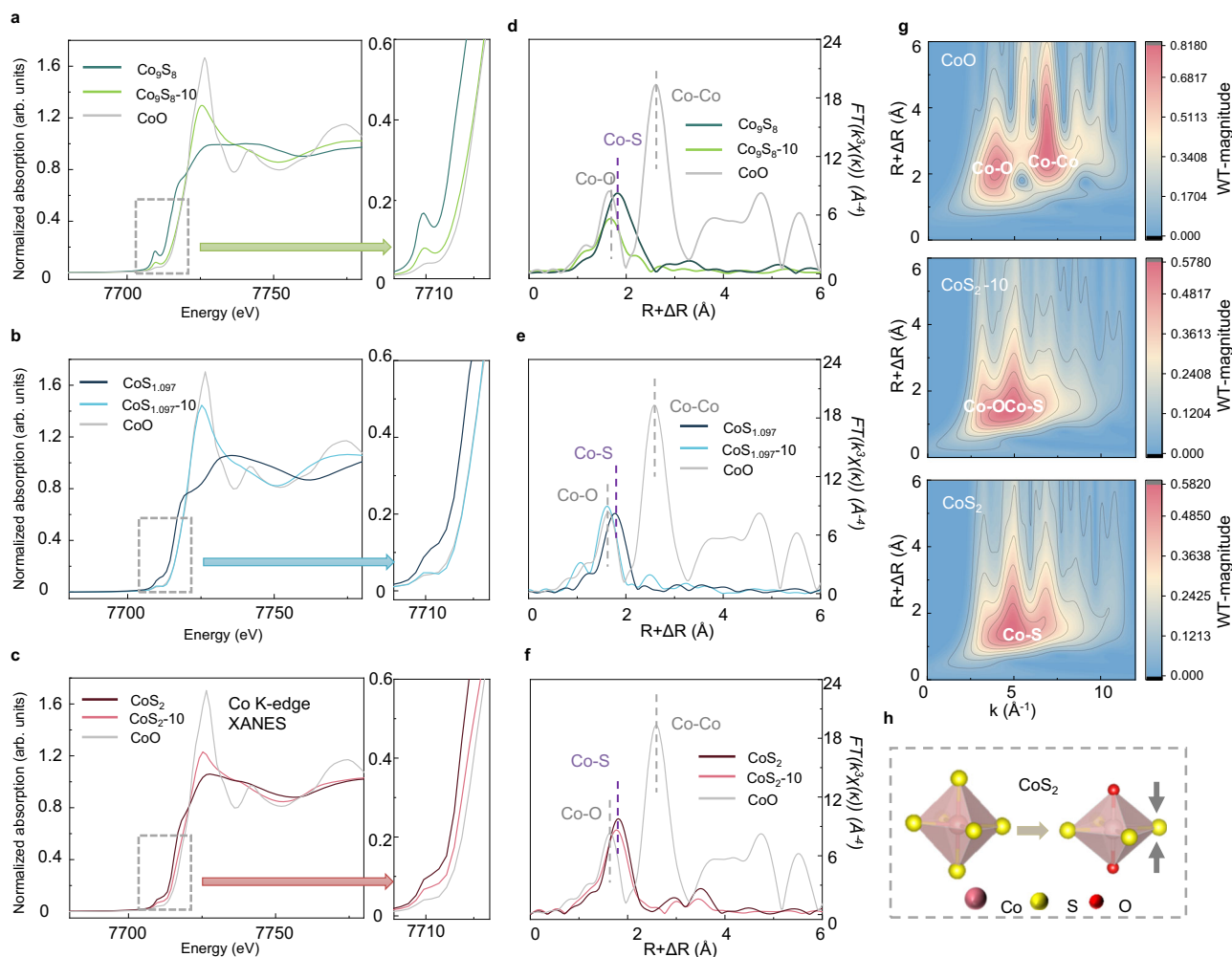


Fig. 2 | The structural evolution characterizations. Co K-edge XANES of **a** Co_9S_8 , **b** $\text{CoS}_{1.097}$, and **c** CoS_2 before and after 10 cycles. Co K-edge FT-EXAFS of **d** Co_9S_8 , **e** $\text{CoS}_{1.097}$, and **f** CoS_2 before and after 10 cycles. **g** WT-EXAFS of CoO, CoS_{2-10} and

CoS_2 . **h** Schematic of structural evolution of CoS_2 during cycling. Source data are provided as a Source Data file.

the $\text{CoS}_{1.097}$ cathodes only have a slight change in 10 cycles. Interestingly, the charge plateau of CoS_2 for 10 cycles is much lower than the pristine one, and the overpotential is reduced from 0.89 V to 0.52 V. These differences prompt our investigation into the CO_2 reaction and real active structure within Li- CO_2 batteries.

The structural evolution characterizations

To investigate structural evolutions that affect the electrochemical behaviors, we performed X-ray photoelectron spectroscopy (XPS) and X-ray absorption spectroscopy (XAS) analyses on the cathodes at different cycles. The XPS results in Supplementary Figs. 8 and 9 indicate that S in CoS_2 has less than the full coordination, which maintains its structure during cycling in Li- CO_2 batteries. In contrast, Co-S bindings decrease significantly in both $\text{CoS}_{1.097}$ and Co_9S_8 , suggesting severe structural changes during cycling. To further confirm the specific structure after cycling, we performed XAS at Co K-edge to study the evolution of Co_9S_8 , $\text{CoS}_{1.097}$, and CoS_2 before and after 10 cycles (labeled as CoS_x-10) in Fig. 2a–c. X-ray absorption near-edge structure (XANES) in Fig. 2a, b show that the absorption edges of Co_9S_8 and $\text{CoS}_{1.097}$ shift to higher energy and overlap with that of CoO after cycling, indicating sulfide oxidation. Fourier transformed extended X-ray absorption fine structures (FT-EXAFS) in Fig. 2d, e show that the first coordination shell of Co_9S_8-10 and $\text{CoS}_{1.097}-10$ is much shorter than that of the pristine samples and are close to that of CoO, confirming most S atoms being substituted by O atoms. In contrast, for

CoS_2 , the absorption edge of CoS_{2-10} is located between that of pristine CoS_2 and CoO, and the first coordination shell of Co is contracted but still longer than that of Co-O (Fig. 2c, f). We compare the FT-EXAFS of CoS_{2-10} with FEFF⁴⁹-calculated Co-O path and Co-S path, showing that the oscillation in the first coordination shell of CoS_2 can not be solely assigned to Co-O scattering or Co-S scattering (Supplementary Fig. 10 a–c). The element of scattering atoms can be derived from EXAFS by the energy dependence of oscillation amplitude⁵⁰. Therefore, we performed inverse Fourier transformation to study the coordination atoms, showing that the first coordination shell is composed of Co-S and Co-O (Supplementary Fig. 10 d–f). Wavelet-transformed EXAFS (WT-EXAFS) shows that the maximum in the region of the first coordination shell is overlapped by Co-O scattering and Co-S scattering, further confirming that Co is coordinated by both S and O in CoS_{2-10} (Fig. 2g). The local structure of Co is quantitatively studied by the least-squares fitting of EXAFS, showing that Co atoms are coordinated by four S atoms at 2.27 Å and two O atoms at 2.00 Å (Supplementary Fig. 11 and Supplementary Table 2). Therefore, we speculate that the CoS_2 is reconstructed to cobalt-oxy sulfide, as shown in Fig. 2h.

CO_2 reduction and evolution reaction mechanism

The cyclic voltammetry (CV) curves of Co_9S_8 , $\text{CoS}_{1.097}$, CoS_2 , and CP in CO_2 and Ar atmosphere are shown in Supplementary Fig. 12. All batteries exhibit featureless curves in the Ar atmosphere while obvious oxidation and reduction peaks in the CO_2 atmosphere, which indicates

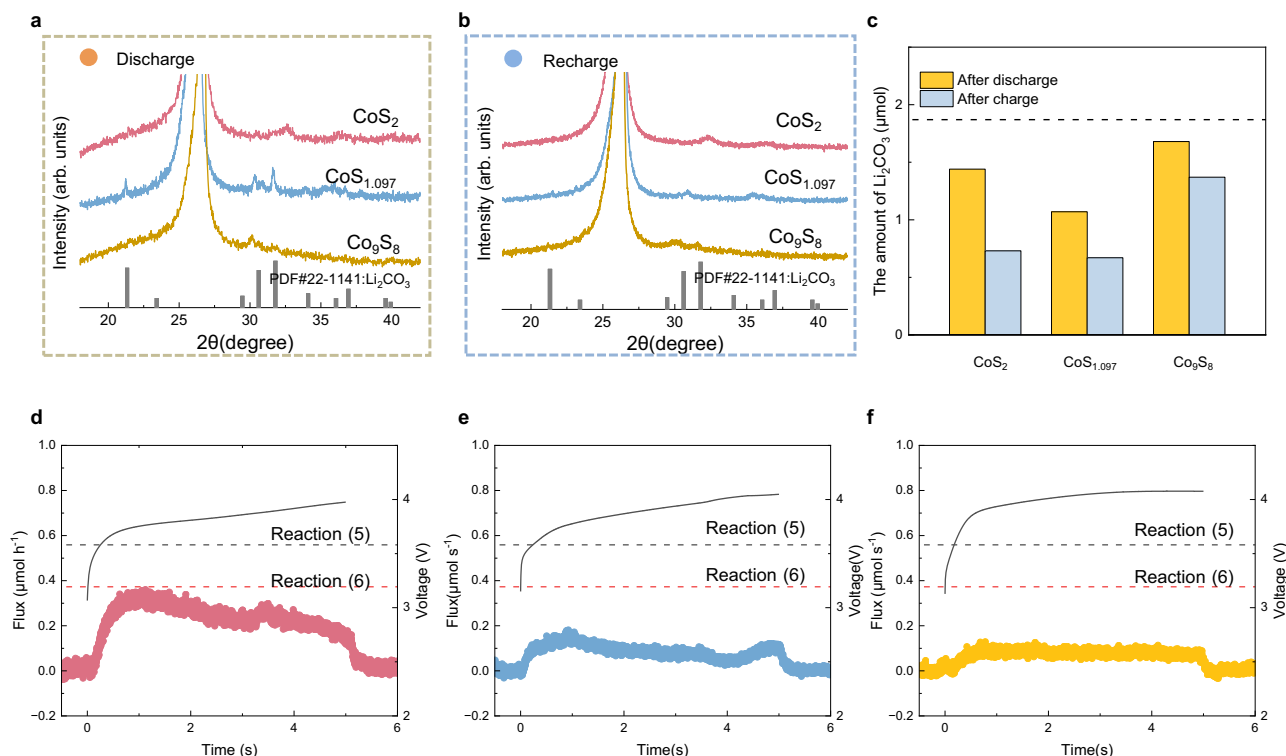


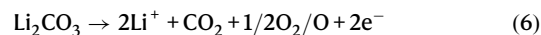
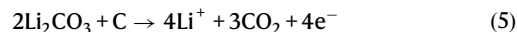
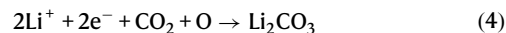
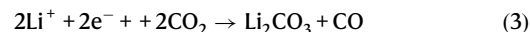
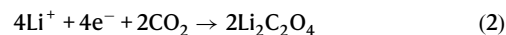
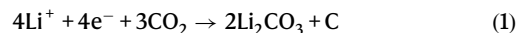
Fig. 3 | CO₂ reduction and evolution reaction mechanism. XRD patterns of the three cathodes for **a** discharging and **b** charging to 200 $\mu\text{A h cm}^{-2}$. **c** The amount of Li₂CO₃ formation and residues on three catalysts after discharge and charge. The dashed line is the theoretical value of Li₂CO₃ formation after discharge. DEMS

results of **d** CoS₂, **e** CoS_{1.097}, and **f** Co₉S₈ during charge at a current density of 20 $\mu\text{A cm}^{-2}$ with a limited capacity of 100 $\mu\text{A h cm}^{-2}$. The dashed lines are the expected flux charge reactions (5) and (6) based on the applied current density. Source data are provided as a Source Data file.

the electrochemical inactivity of sulfides and substrate without CO₂ at the range of 2.2–4.7 V. Therefore, the reactions during discharge and charge mainly rely on CO₂ for the cathodes. To gain mechanistic insight into the electrocatalytic process, ex situ characterizations of products on CoS_x electrodes after discharge and charge were first performed, as shown in Supplementary Fig. 13, including SEM (Supplementary Fig. 14), XRD (Fig. 3a, b), Raman spectroscopy (Supplementary Fig. 15). The SEM images show that the discharge products are large and rodlike covering the surface of CoS_{1.097}, while those on CoS₂ and Co₉S₈ are smaller in Supplementary Fig. 14a–c. The XRD patterns in Fig. 3a show the signal of discharge products can be assigned to Li₂CO₃ (#PDF22-1141) on CoS_{1.097}. After the charge, even though no other peaks are on all cathodes in Fig. 3b, the irregular residues can be easily observed on CoS_{1.097} and Co₉S₈ while those on CoS₂ are not observable in Supplementary Fig. 14d–f. These results roughly indicate that, in comparison with CoS_{1.097} and Co₉S₈, CoS₂ has a higher reversibility. As the discharge products on CoS₂ and Co₉S₈ can not be clearly identified, we infer Li₂CO₃ most probably is the discharge product for the three sulfides based on previous reports and XRD pattern of discharged CoS_{1.097} in Li–CO₂ batteries^{12,51,52}. We also performed Raman spectroscopy in Supplementary Fig. 15 but peaks at 1080 cm⁻¹ corresponding to vibration of Li₂CO₃ are weak on discharged CoS₂ and Co₉S₈.

To verify our assumption and quantify the reversibility for the three catalysts in Li–CO₂ batteries, titration experiments by phosphoric acid are performed on the catalysts after discharge and charge under a current density of 20 $\mu\text{A cm}^{-2}$ with a limited capacity of 100 $\mu\text{A h cm}^{-2}$, which consistent with electrochemical test (Supplementary Fig. 16)⁵³. As shown in Supplementary Fig. 17, CO₂ generation after titrating acid solution on the discharged catalyst, suggesting carbonates, most likely Li₂CO₃ based on the above results, are discharge products on the three catalysts. With external standard 1# in Supplementary Fig. 18 and

Supplementary Table 3, the quantities of formed and residual Li₂CO₃ during discharge and charge on the three cathodes are shown in Fig. 3c and Supplementary Table 4. By now, the reported possible discharge reactions in Li–CO₂ batteries are shown as following reactions (1)–(4)^{9,54–56}. The charge to mass of Li₂CO₃ in all reactions is 2e⁻/Li₂CO₃, including reaction (2) if Li₂C₂O₄ disproportionates to Li₂CO₃. For a 2e⁻/Li₂CO₃ process, -57–89% of the discharge process goes to the formation of Li₂CO₃, indicating Li₂CO₃-related reactions are dominant during discharge for the three sulfides. For charge, there are two possible reactions (5) and (6) with Li₂CO₃ decomposition^{9,43}.



The ratio of Li₂CO₃ and CO₂ is -0.67 for reaction (5) and 1 for reaction (6). In situ differential electrochemical mass spectrometry (DEMS) analysis was performed to calculate CO₂ generation during the charge on the three sulfides. Figure 3d–f and S19 show that only CO₂ (m/z = 44) generation can be observed on all cathodes and the amount of CoS₂ is much higher than that on Co₉S₈ and CoS_{1.097}. As the

numerical results are summarized in Supplementary Table 5, the ratio of Li_2CO_3 to CO_2 of $\text{CoS}_{1.097}$ is 0.85, close to 1, indicating that reaction (6) may mostly happen during charge. Even though no signal of O_2 ($m/z = 32$) has been observed, oxygen species generation is commonly possible and threatens the catalyst's durability⁴³. Consequently, $\text{CoS}_{1.097}$ is oxidized to CoO during cycling and affects its electrochemical performance. The ratio of Co_9S_8 and CoS_2 is -0.76 and -0.56 respectively, close to that of the reaction (5). However, the conversion efficiency of Li_2CO_3 on Co_9S_8 is only 18.4% much lower than the other cathodes, indicating oxidation reactions mainly happened to supply capacity. The XAS results in Fig. 2 show that the valence states of Co in three sulfides maintain +II after 10 cycles, excluding the possibility of Co contribution to the charge capacity. Instead, the sulfur oxidation may be responsible for the charge capacity of Co_9S_8 , as the decreased intensity of Co-S binding in Supplementary Fig. 8a. We also can't exclude the possibility of electrolyte decomposition that supplies the capacity and oxidizes the catalysts. By contrast, the higher charge efficiency of CoS_2 benefits its reconstruction to $\text{Co-S}_4\text{-O}_2$ instead of complete oxidation. We further titrated cathodes after the 9th charge, 10th discharge, and 10th charge to investigate the battery reaction on the reconstructed CoS_2 . As shown in Supplementary Fig. 20, there was little CO_2 generation after titrating the cathodes after the 9th and 10th charge, while an obvious CO_2 generation peak can be observed on the cathode after the 10th discharge, suggesting that most Li_2CO_3 can be decomposed after charge during cycling. Since the measurement values of CO_2 generation on cathodes after the 9th and 10th charge are less than 5% of that on the cathode after the 10th discharge, we approximate the amount of Li_2CO_3 on the cathode after the 10th discharge as the quantities of Li_2CO_3 formation and decomposition in the 10th cycle. Based on external standard 2#, the amount of Li_2CO_3 formation is $-1.15 \mu\text{mol}$, suggesting $\sim 60\%$ charge goes to form Li_2CO_3 during discharge in the 10th cycle (Supplementary Fig. 21 and Supplementary Table 3). These results demonstrate that Li_2CO_3 remains the main discharge product and can be almost completely decomposed during the charge on the reconstructed CoS_2 in cycling.

DFT calculations and discussion

DFT calculations were performed to elucidate the relationship between sulfide structure and activity in Li- CO_2 batteries. Based on our experimental results, we constructed four substrates, including three pre-catalysts Co_9S_8 , $\text{CoS}_{1.097}$, CoS_2 and oxygen partially substituted CoS_2 after cycling (denoted as O- CoS_2 in the latter discussion) in Supplementary Fig. 22. The adsorption energies of CO_2 , Li, and Li_2CO_3 were first calculated to assess the interaction between substrates and reactants during charge and discharge in Li- CO_2 batteries as shown in Supplementary Figs. 23–26^{18,57,58}. As summarized in Fig. 4a and Supplementary Table 6, the adsorption strengths of CO_2 , Li, and Li_2CO_3 on CoS_2 are higher than those on other pre-catalysts, except that the adsorption energy of CO_2 is little weaker than that on Co_9S_8 . Notably, a more negative value of adsorption energies on O- CoS_2 than CoS_2 signifies partial oxygen substitution effectively increases the adsorption strengths. The electronic modulation by O substitution is revealed in Supplementary Fig. 27 and Supplementary Table 7, showing the charge redistribution on neighboring cobalt atoms. A more positive region on O- CoS_2 than CoS_2 suggests that O substitution increases the local polarity and interaction with adsorbed species shown in Fig. 4b. Besides, the *d*-band center of Co shifts to a higher energy level related to the Fermi level due to oxygen substitution, also corresponding with increased adsorption strength of O- CoS_2 (Fig. 4c).

The Gibbs free energies at both open circuit ($U = 0 \text{ V}$) and equilibrium ($U = 2.85 \text{ V}$) potentials for five possible pathways on the four constructed catalysts to further determine the reaction kinetics are shown in Supplementary Figs. 28–32 and Tables S8–II. At the equilibrium potentials, Fig. 4d shows that $^*\text{CO}_3$ and $^*\text{C}$ formation is the rate-

determining step for three pre-catalysts and CoS_2 has the lowest energy difference of this step (2.46 eV) than Co_9S_8 (3.03 eV) and $\text{CoS}_{1.097}$ (3.02 eV). The rate-determining step of O- CoS_2 is changed to step (7) with ΔG (2.14 eV), also lower than that of three pre-catalysts, indicating that partial oxygen substitution further improves the catalytic ability of CoS_2 in Li- CO_2 batteries.

Based on our experimental evidence and DFT results, the structural evolution and consequent change in electrochemical performance are illustrated in Fig. 4d. Co_9S_8 and $\text{CoS}_{1.097}$ as pre-catalysts show serious parasitic reactions during charge in Li- CO_2 batteries. Consequently, the two catalysts have been fully oxidized during cycling, which passivates the catalytic abilities and results in increased overpotentials of batteries. On the contrary, CoS_2 with higher activity shows superior electrochemical performance and reversibility, of which oxidation is terminated and forms oxysulfide with $\text{Co-S}_4\text{-O}_2$ motif in Li- CO_2 batteries. The partial oxygen substitution increases the local polarity and the energy level of the *d*-band center, which adjusts the adsorption strength and thereby reduces the battery overpotential. In short, the initial properties of sulfides play a crucial role in their structural evolutions in batteries and thus affect the performance of batteries during cycling. Our finding also demonstrates the active motifs for reconstructed catalysts, which provide insights for understanding the high activity of sulfides and even other transition compounds.

The application in Li- CO_2 batteries

The high activity of CoS_2 and increased energy efficiency owing to partial oxygen substitution are demonstrated in the latter electrochemical test. The CV curves in Supplementary Fig. 33 show a faster redox reaction rate between CO_2 and C on CoS_2 , with oxidation and reduction currents being higher in comparison to $\text{CoS}_{1.097}$ and Co_9S_8 . The onset potentials for CO_2RR and CO_2ER of three cathodes are compared corresponding to 0.25 mA cm^{-2} shown in Fig. 5a^{10,14}. CoS_2 exhibits more positive and lower potential for CO_2RR (2.76 V) and CO_2ER (4.27 V) in comparison to $\text{CoS}_{1.097}$ (2.69/4.39 V) and Co_9S_8 (2.59/4.42 V), indicating its higher catalytic activities. CoS_2 also shows high reversibility as higher charge capacity ($1781.4 \mu\text{A cm}^{-2}$) and Coulombic efficiency (CE) at 88.8% in the galvanostatic charge-discharge (GDC) test (Fig. 5b), while $\text{CoS}_{1.097}$, Co_9S_8 and CP have charge capacities of 1370.6, 940.0 and $47.7 \mu\text{A cm}^{-2}$ with corresponding CE of 68.8%, 44.2% and 7.2%, respectively.

Figure 5c–e show the rate performance of Li- CO_2 batteries with the three cobalt sulfide cathodes. At the current density of $20 \mu\text{A cm}^{-2}$, the mid-capacity polarizations of CoS_2 , $\text{CoS}_{1.097}$, and Co_9S_8 cathodes are 0.74, 0.91, and 0.75 V, respectively. As the current density increased to $100 \mu\text{A cm}^{-2}$, the overpotentials of the CoS_2 cathode are considerably lower than those of $\text{CoS}_{1.097}$ and Co_9S_8 cathodes, at only 1.19 V, while the overpotentials of the latter cathodes are ramped up significantly to 1.67 and 2.00 V, respectively. When the current density is reverted to $20 \mu\text{A cm}^{-2}$, the overpotential of the CoS_2 cathode reduces to 0.33 V even lower than that of the first three cycles, in contrast to $\text{CoS}_{1.097}$ (1.67 V) and Co_9S_8 (1.63 V) cathodes, which exhibit inferior rate abilities (Supplementary Fig. 34). The cause of this phenomenon has been elucidated above and the same in long-term cycling. Under a current density of $20 \mu\text{A cm}^{-2}$, the overpotential of CoS_2 is significantly reduced and retains stability in cycling as shown in Supplementary Fig. 35a, decreasing to 0.43 V after 400 h, which is also better than other sulfides catalysts (Supplementary Fig. 35b and Supplementary Table 1). Moreover, CoS_2 also maintains a long cycling life of over 700 h and maintains an overpotential lower than 1 V until battery failure (Supplementary Fig. 36 and Fig. 5f). In contrast, the overpotential of batteries with $\text{CoS}_{1.097}$ and Co_9S_8 cathodes exceeds 2 V only after 20 cycles. These

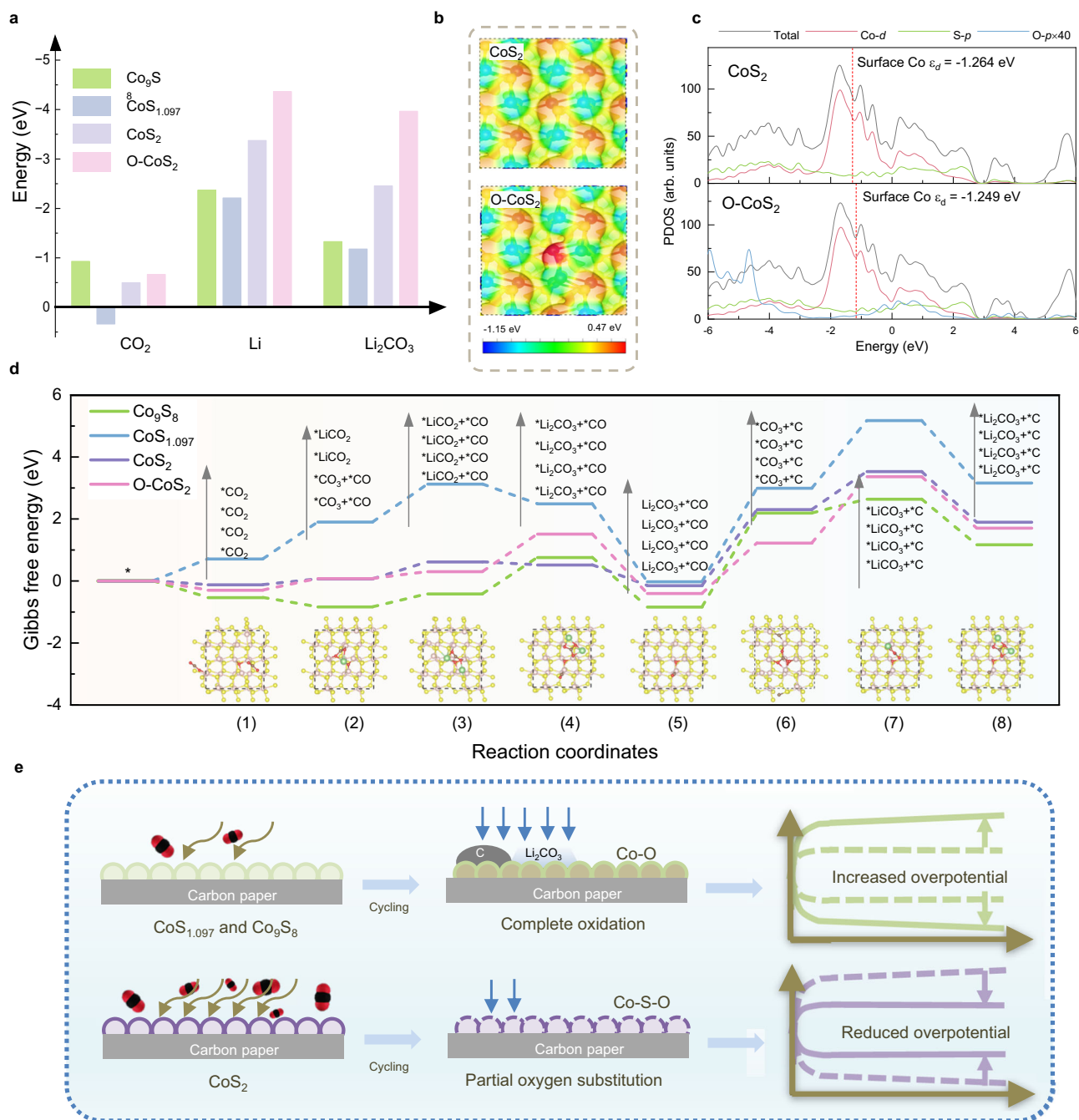


Fig. 4 | DFT calculations and illustration of the reconstruction. **a** The CO_2 , Li, and Li_2CO_3 adsorption energies on Co_9S_8 , $\text{CoS}_{1.097}$, CoS_2 and O-CoS_2 . **b** Surface electrostatic potential diagrams of CoS_2 (up) and O-CoS_2 (down). **c** The projected density of states (PDOS) of CoS_2 (up) and O-CoS_2 (down); the inset red dotted line is the d -band center. **d** Gibbs free energy diagram of reaction pathways in Li-CO_2

batteries at $U = 2.85 \text{ V}$ on the four catalysts. The inset shows the top views of adsorption systems on O-CoS_2 . **e** Illustration of the relationship between structural evolution and activity of CoS_x in Li-CO_2 batteries. Source data are provided as a Source Data file.

contrasts for three cathodes are more visible in the selected cycles in Fig. 5g. Figure 5h shows Li-CO_2 cells based on CoS_2 electrodes with a solar-powered battery and a light-emitting diode (LED) array at day and night, which demonstrates its potential in Mars exploration and operation, where the atmosphere is 96% CO_2 .

In conclusion, we have identified reconstructed motifs and unraveled the structure-activity relations of three cobalt (II) sulfides (CoS_x , $x = 8/9, 1.097, \text{ and } 2$) in Li-CO_2 batteries by combining spectroscopy and DFT calculations. We uncover that most cobalt atoms in Co_9S_8 and $\text{CoS}_{1.097}$ coordinate with oxygen atoms after reconstruction, leading to

their deactivation and degradation in battery performance. In contrast, partial oxygen substitution with the $\text{Co-S}_4\text{-O}_2$ motif in CoS_2 contributes to the charge redistribution on cobalt atoms, thereby improving the catalytic ability. Reconstructed CoS_2 has a high energy efficiency (>80%) and superior stability during cycling with an overpotential of 0.43 V after 400 h in Li-CO_2 batteries. Our finding about active motifs and electronic structure features aids in understanding the high activity of sulfides and other transition compounds catalysts in Li-CO_2 batteries. We also expect our study can pave the way for the development of highly active and stable catalysts for metal-gas batteries.

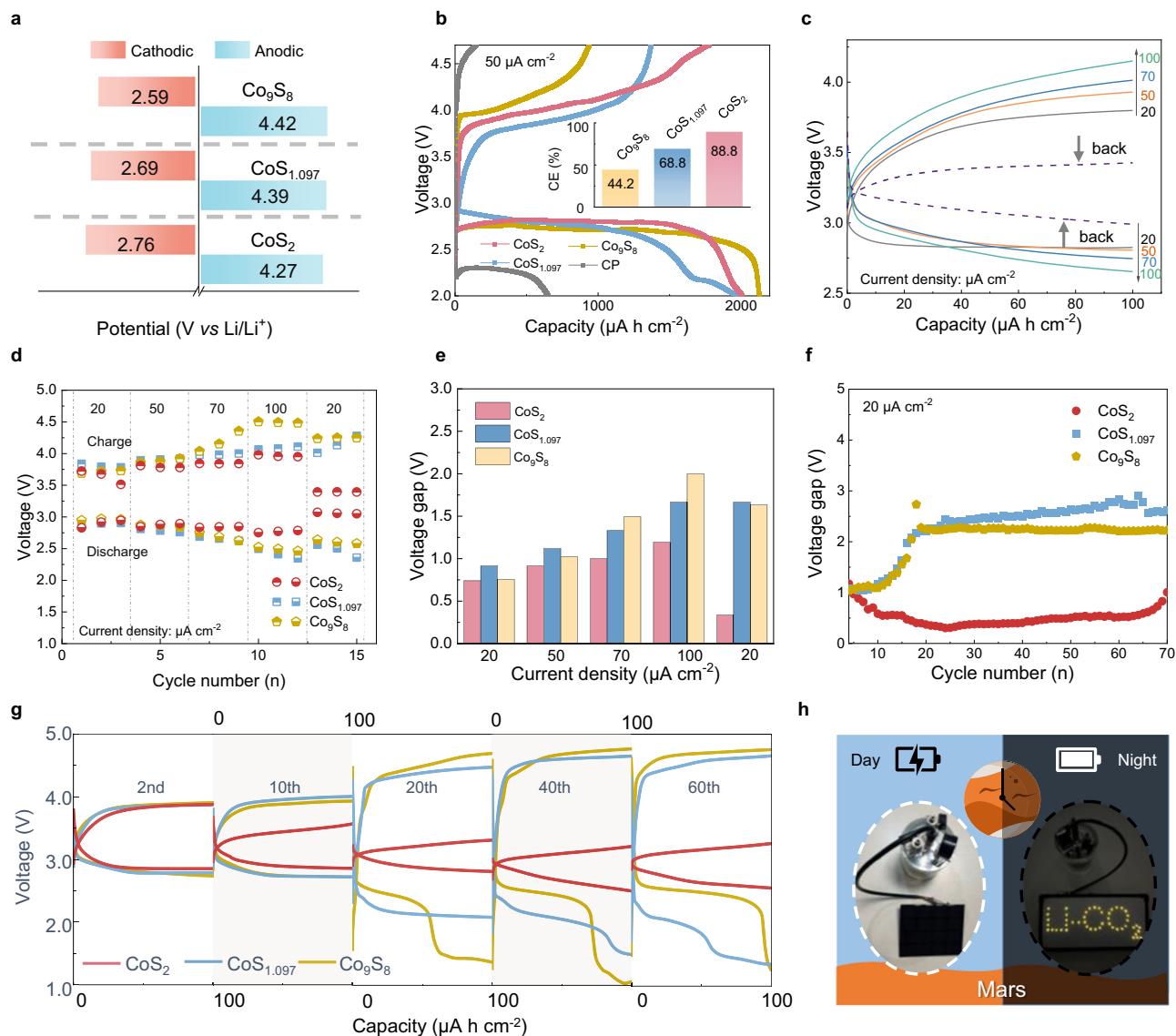


Fig. 5 | Electrochemical performance. **a** The onset potentials during discharge and charge and **b** fully discharging curves at a rate of $50 \mu\text{A cm}^{-2}$ between 2 and 4.7 V (inset is the corresponding CE) for Li-CO₂ batteries with the three cathodes. **c** GDC profiles with a limited capacity of $100 \mu\text{A h cm}^{-2}$ at different current densities for Li-CO₂ battery with the CoS₂ cathode. **d** Discharge and charge voltage and **e** overpotential at different current densities for the three cells. (The value of

overpotential is the average of three cycles with the same current density). **f** The voltage gap of the three cells for long-term cycling. **g** GDC profiles of selected cycles for the three cells. **h** Photo image of a solar-powered battery energy storage system based on Li-CO₂ batteries with CoS₂ cathodes at day and night. Source data are provided as a Source Data file.

Method

Synthesis of free-standing catalysts

Preparation of Co(OH)₂ nanosheets on carbon paper (Co(OH)₂/CP): CP (Toray, H-060) underwent an initial treatment at 700 °C for 10 min to enhance hydrophilicity. Electrodeposition was carried out using a three-electrode system, wherein the pre-treated CP (1 cm²) served as the working electrode, a platinum mesh (1 cm²) acted as the counter electrode, and a saturated calomel electrode (SCE) was used as the reference electrode. The electrolyte solution is 5 mM Co(NO₃)₃·6H₂O. Electrodeposition experiments were conducted using a CHI700E electrochemical workstation at a constant potential of -1.09 V (vs. SCE) for 15 s, followed by a rest period at 0 V (vs. SCE) for 15 s, lasting a total of 40 min. After electrodeposition, the deposited CP was rinsed several times with deionized water and subsequently dried in a vacuum at 60 °C for 12 h.

Preparation of CoS₂/CP: The Co(OH)₂/CP sample was placed at the center of the furnace tube in the quartz boat. 240 mg of S powder was

positioned upstream from the sample. The Co(OH)₂ nanosheets on the CP underwent a reaction with the S powder at 250 °C for 2 h. The temperature was ramped up at a rate of 10 °C per minute. Throughout this process, the environment within the tube was maintained as an Ar/H₂ mixture (5% H₂) flowing at a rate of 100 sccm.

Preparation of CoS_{1.097}/CP: The synthesis method for CoS_{1.097}/CP is similar to that for CoS₂/CP, except for the sulfur powder amount being 120 mg, the temperature being 300 °C, and the time being 2.5 h.

Preparation of Co₉S₈/CP: The synthesized CoS₂/CP was annealed at 300 °C for 1 h with a heating rate of 5 °C min⁻¹ under Ar/H₂(5%) (100 sccm) environment.

Characterization

The morphologies were examined by SEM (Hitachi SU8010) and TEM (FEI Tecnai G2 F30). The cathodes after discharge and charge for SEM were extracted from coin cells, washed by TEGDME in the glovebox, and dried overnight in a vacuum at 60 °C before the test. XRD (Bruker

D8 Advance diffractometer) measurements were conducted to study the composition and structure. XPS spectra were collected using a Kratos AXIS Ultra DLD system to study the chemical states. The XPS results were evaluated with CasaXPS software and calibrated by shifting the main peak in the C 1s spectrum to 284.8 eV assigned to sp^2 carbon. A Pfeiffer QMG 250 DEMS (Germany) was used to measure the ratio of CO_2 evolution and Li_2CO_3 consumption during charge. The developed Li- CO_2 battery is in a homemade Swagelok battery cell (<http://linglush.com>). All electrodes for in situ DEMS test and titration are 1 cm*1 cm for ease of calculation. Lithium metal (diameter of 18 mm), borosilicate glass microfiber (diameter of 22 mm), and 100 μL 1 M lithium bis(trifluoromethane sulfone)imide (LiTFSI) in TEGDME were used as an anode, separator, and electrolyte, respectively. The battery for in situ analysis during charge is under a current density of 20 $\mu\text{A cm}^{-2}$ for 5 h after discharging with the same procedure, and an Ar flux is of 0.8 mL min^{-1} . For titration: cathodes were extracted from their respective Swagelok cells after discharge and charge and dried under vacuum without rinsing. They were then placed in a custom-built vessel (<http://linglush.com>). The 2 capillaries were attached to the DEMS apparatus and Ar through the vessel with a flux of 0.25 mL min^{-1} . After establishing a stable CO_2 and O_2 baseline, 1 mL of 3 M H_3PO_4 was injected into the vessel through a septa seal. The total amount of CO_2 evolved was calculated by integrating CO_2 flux. The CO_2 flux is determined as $\text{ppm}(\text{CO}_2/\text{Ar}) \cdot 0.25 \text{ mL min}^{-1} / 22.4 \text{ L mol}^{-1}$. The DEMS cell was controlled by a LAND system.

Electrochemical measurements

Coin cells (CR 2032) with several holes in the cathode were used to investigate the electrochemical performance of the Li- CO_2 batteries. Freestanding CoS_2/CP , $\text{CoS}_{1.097}/\text{CP}$, and $\text{Co}_9\text{S}_8/\text{CP}$ (1 cm*1 cm) were directly used as the cathodes. Lithium metal, borosilicate glass microfiber (diameter of 18 mm), and 100 μL 1 M lithium bis(trifluoromethane sulfone)imide (LiTFSI) in TEGDME were used as an anode, separator, and electrolyte, respectively. The cells were assembled in an Ar-filled glovebox. Then they are transferred into chambers with pure CO_2 for electrochemical test. An electrochemical workstation Biologic SPI50 and a LAND CT 2001A testing system were used to obtain the CV and discharge-charge curves, respectively. Because the potential of Li foil is easily affected by SEI and electrolytes, commercial LiFePO_4 electrodes are much more stable (aluminum foil single-side coated LiFePO_4 electrode, active material loading: 120 g/m^2) were used for the CV test⁵⁹. ECSA measurement: The comparison of ECSA for cathodes was calculated based on C_{dl} , which is the double-layer capacitance. C_{dl} was defined as $C_{\text{dl}} = (i_a - i_c) / 2v$, i_a is the anodic current, and i_c is the cathodic current. v is the scan rate of CVs in the non-faradaic region, an area between -0.26 – -0.16 V of the open circuit potential (OCP). C_{dl} was obtained by plotting $(i_a - i_c) / 2$ as a function of v . All electrochemical tests are carried out in the room temperature.

XAS measurements

The XAS spectra at the Co K-edges were recorded at the BL11B beamline of the Shanghai Synchrotron Radiation Facility (SSRF). The storage ring was operated at 3.5 GeV with a beam current of 200 mA in a top-up mode. The incident photons were monochromatized by a Si (111) double-crystal monochromator, with an energy resolution $\Delta E/E = 1.4 \times 10^{-4}$. The spot size at the sample was $\sim 200 \mu\text{m} \times 250 \mu\text{m}$ ($H \times V$). The XAS spectra of the samples at Co K-edges were calibrated by the Co reference foils (edge energy 7709 eV) collected in transition mode. The XAS spectra of the samples were collected in fluorescence mode, with a Lytle ionization chamber filled with Ar.

XAFS data analysis

The data of XAFS were processed with ATHENA software implemented in the IFEFFIT software packages⁶⁰. The raw data of XAFS were background subtracted from the overall absorption and then normalized

regarding the edge-jump step. Next, the k^3 -weighted $\chi(k)$ data of Co K-edge were Fourier transformed to R space using a Hanning window ($dk = 1.0 \text{ \AA}^{-1}$) in k -space, which separates the contributions of different coordination shells to the EXAFS data. EXAFS of Co K-edge were Fourier transformed between 2.398 and 11.150 \AA^{-1} . The quantitative structure parameters of Fe were obtained by least-squares fitting of EXAFS data with ATERMIS software in the IFEFFIT software packages. The fitting was according to the EXAFS Eq. (1):

$$\chi(k) = \sum_i \frac{N_i S_0^2 F_i(k)}{k R_i^2} \sin(2kR_i + \varphi_i(k)) e^{-\frac{2R_i}{\lambda(k)}} e^{-2\sigma_i^2 k^2} \quad (7)$$

where $F_i(k)$, the effective scattering amplitude, $\lambda(k)$ the mean free path, and $\varphi_i(k)$, the effective scattering phase shift were theoretically calculated by the ab-initio code FEFF 6⁴⁹. The fitting was conducted in R space with the single scattering path of the first coordination shells.

The wavelet transformations of k^2 -weighted EXAFS of Co K-edge were performed in the k range between 2.50 and 11.50 \AA^{-1} with a k step of 0.05 \AA^{-1} and the R range between 0 and 6 \AA with the hamaFortran program by using the Morlet wavelets⁶¹:

$$\varphi(k) = \frac{1}{\sqrt{2\pi}\sigma} e^{-\frac{k^2}{2\sigma^2}} (e^{i\omega k} - e^{-\frac{k^2}{2}}) \quad (8)$$

Where ω is the frequency and σ is the half-width. To get a high resolution at the k -axis in the region of the first coordination shell, we chose $\omega = 3.5$ and $\sigma = 0.5$ for CoS_2 and CoS_2 -10, and $\omega = 1$ and $\sigma = 1$ for CoO , respectively.

Computation method

The first principles calculations were performed using the Vienna ab initio simulation package 6.4.0⁶². A plane-wave cutoff energy of 400 eV was used. The generalized gradient approximation proposed by Perdew, Burke, and Ernzerhof was used in the projector augmented wave method^{63,64}. The computationally cost-effective Grimme's D3 scheme method for van der Waals (vdW) interactions was used to obtain a clear picture of weak interaction⁶⁵. $\text{Co}_9\text{S}_8(311)$, $\text{CoS}_{1.097}(204)$, $\text{CoS}_2(100)$ and $\text{O-CoS}_2(100)$ were constructed. The detailed structural models can be found in Supplementary Data 1. Due to periodic boundary conditions, a vacuum separation of 20 \AA between two neighboring monolayers was used. For the optimization and self-consistent calculations of surfaces, the Brillouin zone was sampled using the Monkhorst-Pack scheme with 0.05 of k -spacing value, respectively⁶⁶. Ionic and electronic relaxations were performed by applying a convergence criterion of 0.05 eV/ \AA per ion and 10^{-5} eV per electronic step, respectively. Here the dipole correction for slabs were considered in calculation. The Gibbs free energies (G) of each reaction intermediate were given by following Eq. (3):

$$G = E_{\text{DFT}} + E_{\text{ZPE}} - TS \quad (8)$$

where E_{DFT} , E_{ZPE} , T , and S are total energy by DFT calculations, the zero-point energy, temperature (298.15 K), and entropy, respectively. The entropies of other adsorbed molecules (ΔS) are calculated from the vibrational frequencies associated with the normal modes in the harmonic approximation.

The adsorption energy equals the energy of the adsorbed system minus the total energy of the substrate and the independent molecule or atom. The more negative the adsorption energy, the stronger the adsorption. By the Nernst equation, the calculated theoretical equilibrium potential U_0 is 2.85 V for $2 \text{ Li (s)} + 3/2 \text{ CO}_2 \text{ (g)} \rightarrow \text{Li}_2\text{CO}_3 \text{ (s)} + 1/2 \text{ C (s)}$, which is comparable to previous result^{14,67}.

Data availability

All data that support the findings of this study are presented in the Manuscript and Supplementary Information, or are available from the corresponding author upon request. Source data are provided with this paper.

References

- Wei, D., Sang, R., Sponholz, P., Junge, H. & Beller, M. Reversible hydrogenation of carbon dioxide to formic acid using a Mn-pincer complex in the presence of lysine. *Nat. Energy* **7**, 438–447 (2022).
- Wang, F. et al. Metal–CO₂ electrochemistry: from CO₂ recycling to energy storage. *Adv. Energy Mater.* **11**, 2100667 (2021).
- Liu, Y. et al. Atomic design of bidirectional electrocatalysts for reversible Li–CO₂ batteries. *Mater. Today* **63**, 120–136 (2023).
- Ross, M. B. et al. Designing materials for electrochemical carbon dioxide recycling. *Nat. Catal.* **2**, 648–658 (2019).
- Guan, D.-H. et al. Light/electricity energy conversion and storage for a hierarchical porous In₂S₃@CNT/SS cathode towards a flexible Li–CO₂ battery. *Angew. Chem. Int. Ed.* **59**, 19518–19524 (2020).
- Guan, D.-H. et al. All-solid-state photo-assisted Li–CO₂ battery working at an ultra-wide operation temperature. *ACS Nano* **16**, 12364–12376 (2022).
- Chen, B. et al. Engineering the active sites of graphene catalyst: from CO₂ activation to activate Li–CO₂ batteries. *ACS Nano* **15**, 9841–9850 (2021).
- Yang, S. et al. A reversible lithium–CO₂ battery with Ru nanoparticles as a cathode catalyst. *Energy Environ. Sci.* **10**, 972–978 (2017).
- Qiao, Y. et al. Li–CO₂ electrochemistry: a new strategy for CO₂ fixation and energy storage. *Joule* **1**, 359–370 (2017).
- Lu, B. et al. Engineering the interfacial orientation of MoS₂/Co₉S₈ bidirectional catalysts with highly exposed active sites for reversible Li–CO₂ batteries. *Proc. Natl Acad. Sci. USA* **120**, e2216933120 (2023).
- Qi, G., Zhang, J., Chen, L., Wang, B. & Cheng, J. Binder-free mononanofibers catalysts for flexible 2-electron oxalate-based Li–CO₂ batteries with high energy efficiency. *Adv. Funct. Mater.* **32**, 2112501 (2022).
- Zhang, Z., Bai, W.-L., Wang, K.-X. & Chen, J.-S. Electrocatalyst design for aprotic Li–CO₂ batteries. *Energy Environ. Sci.* **13**, 4717–4737 (2020).
- Chen, B., Zhong, X., Zhou, G., Zhao, N. & Cheng, H.-M. Graphene-supported atomically dispersed metals as bifunctional catalysts for next-generation batteries based on conversion reactions. *Adv. Mater.* **34**, 2105812 (2022).
- Chen, B. et al. Designing electrophilic and nucleophilic dual centers in the ReS₂ plane toward efficient bifunctional catalysts for Li–CO₂ batteries. *J. Am. Chem. Soc.* **144**, 3106–3116 (2022).
- Chen, C. J. et al. Catalytically active site identification of molybdenum disulfide as gas cathode in a nonaqueous Li–CO₂ battery. *ACS Appl. Mater. Interfaces* **13**, 6156–6167 (2021).
- Ahmadiparidari, A. et al. A long-cycle-life lithium–CO₂ battery with carbon neutrality. *Adv. Mater.* **31**, 1902518 (2019).
- Jin, Y. et al. Interfacial engineering in hollow NiS₂/FeS₂-NSGA heterostructures with efficient catalytic activity for advanced Li–CO₂ battery. *Chem. Eng. J.* **430**, 133029 (2022).
- Wang, H. et al. Realizing interfacial electronic interaction within ZnS quantum Dots/N-rGO heterostructures for efficient Li–CO₂ batteries. *Adv. Energy Mater.* **9**, 1901806 (2019).
- Pipes, R., He, J., Bhargava, A. & Manthiram, A. Efficient Li–CO₂ batteries with molybdenum disulfide nanosheets on carbon nanotubes as a catalyst. *ACS Appl. Energy Mater.* **2**, 8685–8694 (2019).
- Li, X. et al. Bamboo-like nitrogen-doped carbon nanotube forests as durable metal-free catalysts for self-powered flexible Li–CO₂ batteries. *Adv. Mater.* **31**, 1903852 (2019).
- Song, L. et al. An ultra-long life, high-performance, flexible Li–CO₂ battery based on multifunctional carbon electrocatalysts. *Nano Energy* **71**, 104595 (2020).
- Xiao, Y. et al. High-performance Li–CO₂ batteries from free-standing, binder-free, bifunctional three-dimensional carbon catalysts. *ACS Energy Lett.* **5**, 916–921 (2020).
- Li, Y. et al. Highly surface-wrinkled and N-doped CNTs anchored on metal wire: a novel fiber-shaped cathode toward high-performance flexible Li–CO₂ batteries. *Adv. Funct. Mater.* **29**, 1808117 (2019).
- Liu, Y. et al. Toward an understanding of the reversible Li–CO₂ batteries over metal–N₄-functionalized graphene electrocatalysts. *ACS Nano* **16**, 1523–1532 (2022).
- Lin, J. et al. Boosting energy efficiency and stability of Li–CO₂ batteries via synergy between Ru atom clusters and single-atom Ru–N₄ sites in the electrocatalyst cathode. *Adv. Mater.* **34**, 2200559 (2022).
- Hu, C. et al. High-performance, long-life, rechargeable Li–CO₂ batteries based on a 3D holey graphene cathode implanted with single iron atoms. *Adv. Mater.* **32**, 1907436 (2020).
- Zhang, B. W. et al. Targeted synergy between adjacent Co atoms on graphene oxide as an efficient new electrocatalyst for Li–CO₂ batteries. *Adv. Funct. Mater.* **29**, 1904206 (2019).
- Wu, G. et al. Design of ultralong-life Li–CO₂ batteries with IrO₂ nanoparticles highly dispersed on nitrogen-doped carbon nanotubes. *J. Mater. Chem. A* **8**, 3763–3770 (2020).
- Xiao, X. et al. Ultrafine Co-doped NiO nanoparticles decorated on carbon nanotubes improving the electrochemical performance and cycling stability of Li–CO₂ batteries. *ACS Appl. Energy Mater.* **4**, 11858–11866 (2021).
- Zheng, R. et al. Oxygen vacancy engineering of vertically aligned NiO nanosheets for effective CO₂ reduction and capture in Li–CO₂ battery. *Electrochim. Acta* **383**, 138359 (2021).
- Ma, W., Lu, S., Lei, X., Liu, X. & Ding, Y. Porous Mn₂O₃ cathode for highly durable Li–CO₂ batteries. *J. Mater. Chem. A* **6**, 20829–20835 (2018).
- Zhang, X. et al. High performance Li–CO₂ batteries with NiO–CNT cathodes. *J. Mater. Chem. A* **6**, 2792–2796 (2018).
- Lei, D., Ma, S., Lu, Y., Liu, Q. & Li, Z. High-performance Li–CO₂ batteries with α-MnO₂/CNT cathodes. *J. Electron. Mater.* **48**, 4653–4659 (2019).
- Wang, C. et al. Fabricating Ir/C nanofiber networks as free-standing air cathodes for rechargeable Li–CO₂ batteries. *Small* **14**, 1800641 (2018).
- Xing, Y. et al. Crumpled Ir nanosheets fully covered on porous carbon nanofibers for long-life rechargeable lithium–CO₂ batteries. *Adv. Mater.* **30**, 1803124 (2018).
- Fan, L. et al. Biaxially compressive strain in Ni/Ru core/shell nanoplates boosts Li–CO₂ batteries. *Adv. Mater.* **34**, 2204134 (2022).
- Qiao, Y. et al. Synergistic effect of bifunctional catalytic sites and defect engineering for high-performance Li–CO₂ batteries. *Energy Storage Mater.* **27**, 133–139 (2020).
- Qiao, Y. et al. Transient, in situ synthesis of ultrafine ruthenium nanoparticles for a high-rate Li–CO₂ battery. *Energy Environ. Sci.* **12**, 1100–1107 (2019).
- Qiao, Y. et al. 3D-printed graphene oxide framework with thermal shock synthesized nanoparticles for Li–CO₂ batteries. *Adv. Funct. Mater.* **28**, 1805899 (2018).
- Jin Y., Chen F., Wang J. & Johnston R. L. Tuning electronic and composition effects in ruthenium-copper alloy nanoparticles

- anchored on carbon nanofibers for rechargeable Li-CO₂ batteries. *Chem. Eng. J.* **375**, 121978 (2019).
41. Chen, L. et al. Copper indium sulfide enables Li-CO₂ batteries with boosted reaction kinetics and cycling stability. *Energy Environ. Mater.* **0**, 1–9 (2022).
 42. Cao, D., Tan, C. & Chen, Y. Oxidative decomposition mechanisms of lithium carbonate on carbon substrates in lithium battery chemistries. *Nat. Commun.* **13**, 4908 (2022).
 43. Mahne, N., Renfrew, S. E., McCloskey, B. D. & Freunberger, S. A. Electrochemical oxidation of lithium carbonate generates singlet oxygen. *Angew. Chem. Int. Ed.* **57**, 5529–5533 (2018).
 44. Tan, C. et al. Unravelling the complex Na₂CO₃ electrochemical process in rechargeable Na-CO₂ batteries. *Adv. Energy Mater.* **13**, 2204191 (2023).
 45. Yang, S., He, P. & Zhou, H. Exploring the electrochemical reaction mechanism of carbonate oxidation in Li-air/CO₂ battery through tracing missing oxygen. *Energy Environ. Sci.* **9**, 1650–1654 (2016).
 46. Ishikawa, A. et al. Oxysulfide Sm₂Ti₂S₂O₅ as a stable photocatalyst for water oxidation and reduction under visible light irradiation ($\lambda \leq 650$ nm). *J. Am. Chem. Soc.* **124**, 13547–13553 (2002).
 47. Wang, Q. et al. Oxysulfide photocatalyst for visible-light-driven overall water splitting. *Nat. Mater.* **18**, 827–832 (2019).
 48. Yoon, S. B. et al. Graphitized pitch-based carbons with ordered nanopores synthesized by using colloidal crystals as templates. *J. Am. Chem. Soc.* **127**, 4188–4189 (2005).
 49. Rehr, J. J. & Albers, R. C. Theoretical approaches to x-ray absorption fine structure. *Rev. Mod. Phys.* **72**, 621–654 (2000).
 50. Teo B. K. Theoretical amplitude and phase functions. In: *EXAFS: Basic Principles and Data Analysis* (ed. Teo, B. K.) (Springer Berlin Heidelberg, 1986).
 51. Xie, Z., Zhang, X., Zhang, Z. & Zhou, Z. Metal-CO₂ batteries on the road: CO₂ from contamination gas to energy source. *Adv. Mater.* **29**, 1605891 (2017).
 52. Mu, X., Pan, H., He, P. & Zhou, H. Li-CO₂ and Na-CO₂ batteries: toward greener and sustainable electrical energy storage. *Adv. Mater.* **32**, 1903790 (2020).
 53. McCloskey, B. D. et al. Combining accurate O₂ and Li₂O₂ assays to separate discharge and charge stability limitations in nonaqueous Li-O₂ batteries. *J. Phys. Chem. Lett.* **4**, 2989–2993 (2013).
 54. Xu, S., Das, S. K. & Archer, L. A. The Li-CO₂ battery: a novel method for CO₂ capture and utilization. *RSC Adv.* **3**, 6656–6660 (2013).
 55. Xie, J., Liu, Q., Huang, Y., Wu, M. & Wang, Y. A porous Zn cathode for Li-CO₂ batteries generating fuel-gas CO. *J. Mater. Chem. A* **6**, 13952–13958 (2018).
 56. Hou, Y. et al. Mo₂C/CNT: an efficient catalyst for rechargeable Li-CO₂ batteries. *Adv. Funct. Mater.* **27**, 1700564 (2017).
 57. Zhang, X. et al. Breaking the stable triangle of carbonate via W-O bonds for Li-CO₂ batteries with low polarization. *ACS Energy Lett.* **6**, 3503–3510 (2021).
 58. Ye, F. et al. Topological defect-rich carbon as a metal-free cathode catalyst for high-performance Li-CO₂ batteries. *Adv. Energy Mater.* **11**, 2101390 (2021).
 59. Murdock, B. E., Armstrong, C. G., Smith, D. E., Tapia-Ruiz, N. & Toghiani, K. E. Misreported non-aqueous reference potentials: the battery research endemic. *Joule* **6**, 928–934 (2022).
 60. Newville, B. R. M. ATHENA, ARTEMIS, HEPHAESTUS: data analysis for X-ray absorption spectroscopy using IFFFIT. *J. Synchrotron Radiat.* **12**, 537–541 (2005).
 61. Funke H., Scheinost A. C., Chukalina M. Wavelet analysis of extended x-ray absorption fine structure data. *Phys. Rev. B* **71**, 094110 (2005).
 62. Kresse, G. & Furthmüller, J. Efficient iterative schemes for ab initio total-energy calculations using a plane-wave basis set. *Phys. Rev. B* **54**, 11169–11186 (1996).
 63. Kresse, G. & Joubert, D. From ultrasoft pseudopotentials to the projector augmented-wave method. *Phys. Rev. B* **59**, 1758–1775 (1999).
 64. Perdew, J. P., Burke, K. & Ernzerhof, M. Generalized gradient approximation made simple. *Phys. Rev. Lett.* **77**, 3865–3868 (1996).
 65. Grimme, S., Antony, J., Ehrlich, S. & Krieg, H. A consistent and accurate ab initio parametrization of density functional dispersion correction (DFT-D) for the 94 elements H-Pu. *J. Chem. Phys.* **132**, 154104 (2010).
 66. Monkhorst, H. J. & Pack, J. D. Special points for Brillouin-zone integrations. *Phys. Rev. B* **13**, 5188–5192 (1976).
 67. Yang, C., Guo, K., Yuan, D., Cheng, J. & Wang, B. Unraveling reaction mechanisms of Mo₂C as cathode catalyst in a Li-CO₂ battery. *J. Am. Chem. Soc.* **142**, 6983–6990 (2020).

Acknowledgements

This work was supported by the Joint Funds of the National Natural Science Foundation of China (U21A20174)[G.Z.], Guangdong Innovative and Entrepreneurial Research Team Program (2021ZT09L197) [G.Z.], Shenzhen Science and Technology Program (KQTD20210811090112002) [G.Z.], Shenzhen Stabilization Support Program (WDZC20200824091903001) [G.Z.], Guangdong Basic and Applied Basic Research Foundation (2020B0301030002) [H.-M.C.], the start-up funds, Overseas Research Cooperation Fund, and Interdisciplinary Research and Innovation Fund of Tsinghua Shenzhen International Graduate School, and China Postdoctoral Science Foundation (No. 2020TQ0159) [B.C.]. We also thank the staff in the BL11B beamline at Shanghai Synchrotron Radiation Facility (SSRF) for their technical assistance and Prof. Ji-Jing Xu and Mr. Dehui Guan from Jilin University for their support in the DEMS tests.

Author contributions

Y.L., G.Z., and H.-M.C. conceived the idea for this project. Y.L. prepared the materials and electrochemical measurements. Z.Z. and B.L.L. carried out the XAS measurements and data analysis. D.W. conducted the DFT calculations and discussed the results. J.T. and B.L.L. performed the TEM test. B.C., B.Y.L., and R.M. assisted with battery testing and material synthesis. Y.L., D.W., Z.Z., G.Z., and H.-M.C. co-wrote the paper.

Competing interests

The authors declare no competing interests.

Additional information

Supplementary information The online version contains supplementary material available at <https://doi.org/10.1038/s41467-024-46465-8>.

Correspondence and requests for materials should be addressed to Dashuai Wang, Guangmin Zhou or Hui-Ming Cheng.

Peer review information *Nature Communications* thanks Graham Leverick, Xingbao Zhu, and the other anonymous reviewer(s) for their contribution to the peer review of this work. A peer review file is available.

Reprints and permissions information is available at <http://www.nature.com/reprints>

Publisher's note Springer Nature remains neutral with regard to jurisdictional claims in published maps and institutional affiliations.

Open Access This article is licensed under a Creative Commons Attribution 4.0 International License, which permits use, sharing, adaptation, distribution and reproduction in any medium or format, as long as you give appropriate credit to the original author(s) and the source, provide a link to the Creative Commons licence, and indicate if changes were made. The images or other third party material in this article are included in the article's Creative Commons licence, unless indicated otherwise in a credit line to the material. If material is not included in the article's Creative Commons licence and your intended use is not permitted by statutory regulation or exceeds the permitted use, you will need to obtain permission directly from the copyright holder. To view a copy of this licence, visit <http://creativecommons.org/licenses/by/4.0/>.

© The Author(s) 2024